Actin and Microtubules Position Stress Granules

Thomas J. Böddeker, [1,*] Anja Rusch, [1] Keno Leeners, [1] Michael P. Murrell, [2] and Eric R. Dufresne [1,3,†]
[1] *Department of Materials, ETH Zurich, 8093 Zurich, Switzerland*
[2] *Department of Biomedical Engineering, Yale University, New Haven, Connecticut 06510, USA*
[3] *Department of Physics, Department of Materials Science and Engineering, Cornell University, Ithaca, New York 14850, USA*

(Received 24 March 2023; accepted 17 November 2023; published 19 December 2023)

Membraneless organelles, liquidlike condensates composed of protein and nucleic acids, alter the biochemical and physical landscape of the cell. While specific membraneless organelles are found in stereotypical locations, little is known about the physical mechanisms that guide their positioning. Here, we investigate how stress granules, a type of cytoplasmic membraneless organelle, establish their stereotypical perinuclear positioning. We find that actin and microtubules play complementary roles. Lamellar actin confines stress granules, and its retrograde flow drives them toward the cell center. Microtubules, in turn, adhere to stress granules through capillary interactions, which tend to concentrate stress granules in microtubule-rich regions near the nucleus. Similar physical mechanisms are likely to play a role in the positioning of other membraneless organelles.

DOI: 10.1103/PRXLife.1.023010

I. INTRODUCTION

To survive and proliferate, cells need to regulate a vast number of biochemical reactions. To facilitate this daunting task, cells compartmentalize many of these reactions within organelles, including membrane-enclosed organelles (such as mitochondria or endoplasmic reticula), or membraneless organelles (such as the nucleolus in the nucleus or stress granules and p-bodies in the cytoplasm) [1]. The function of membrane-enclosed organelles has been shown to depend on their position within the cell, with an impact on signaling, cell polarization, or growth [2]. Positioning of membrane-enclosed organelles is often assisted by active mechanisms, such as motor-driven transport along cytoskeletal filaments [2–6].

Less is known about motion and positioning of membraneless organelles in the cytoplasm. These biomolecular condensates are typically composed of protein and mRNA [1,7]. Stress granules (SGs) are cytoplasmic membraneless organelles that serve as dynamic sites of mRNA sorting. They are important for reorganization of translation under biological stress (e.g., exposure to toxic chemicals or heat) [8–10]. Because the formation of SGs can easily be induced by stress, they are a convenient model system to study the appearance and localization of membraneless organelles in the cytoplasm. A key protein for SG formation under oxidative stress, such as caused by exposure to arsenite, is G3BP1 [11,12]. In unperturbed cells, G3BP1, as well as other SG components, are dispersed in the cytosol. Upon exposure to stress, these macromolecules condense to form SGs throughout the cytoplasm before migrating toward the cell center [8,13,14]. Ultimately, SGs are found in the microtubule-rich perinuclear region of the cytoplasm [15,16]. As SGs travel towards the nucleus, they coalesce and grow, resulting in several micron-sized granules within tens of minutes of exposure to stress [13,14,17].

The localization of condensates in a complex environment can be controlled by several mechanisms. Cells may localize droplet nucleation to defined regions of the cell through spatial gradients in protein concentration [18–20] or temperature [21]. In mammalian cells, and human bone osteosarcoma epithelial (U2OS) cells used in this study in particular, we find that SGs, however, form throughout the entire cytoplasm and subsequently migrate. Another reported mechanism is to steer condensation and droplet migration by gradients in stiffness of the surrounding material [22,23]. Material properties of the cytoplasm, however, are heterogeneous on the lengthscale of SGs, and viscoelasticity of the cytoplasm leads to relaxation of many mechanical constraints within minutes [24]. These considerations suggest that other intracellular mechanisms or interactions must be at play that orchestrate the positioning of SGs.

Cytoskeletal components are obvious suspects for the active control of the position of membraneless organelles. Microtubules have indeed been suggested to aid stress granule formation by acting as tracks for active transport of granule components through motor proteins [25–29] and by encouraging droplet fusion through mixing of the cytoplasm through their dynamic instability [30]. Early studies reported that microtubules are necessary for the formation of stress granules [25,26], while more recent work found that SGs readily form in the absence of a microtubule network [13,14,31]. Similarly, a microtubule-associated motor, dynein, has been reported as a critical component for SGs in neurons [28], whereas other work found that dynein has no impact on SG formation in epithelial cells [14]. Association of SGs to other cellular structures may explain previously observed instances of

---

[*] Current address: Institute of Biology, Humboldt-Universität zu Berlin, 10115 Berlin, Germany.

[†] eric.r.dufresne@cornell.edu

ballistic transport of SGs. p-bodies are known to both associate with SGs [11,32] and to be actively transported along microtubules [33]. Similarly, SGs have been shown to associate with lysosomes that are transported along microtubules for long-distance transport in neurons [34]. Disruption of the actin network, on the other hand, has been reported to have no effect on SG formation [26,29]. Overall, these studies, albeit at times contradictory, suggest that the cytoskeleton and associated proteins influence SG positioning.

Here, we investigate the potential impact of actin and microtubules on the positioning of SGs using novel quantitative methods. Combining quantitative structural measurements in fixed cells with live cell dynamics and cytoskeletal perturbations, we find conclusive evidence that both actin and microtubules impact SG dynamics and identify distinct roles for actin and microtubules. Lamellar actin confines SGs, and its retrograde flow transports them toward the cell center. Once there, microtubules guide SGs to their final location through attractive capillary interactions. The localization of SGs within the cell is therefore a consequence of SGs interacting with the dynamic and heterogeneous environment of the cytoplasm. These generic physical mechanisms are also likely to play a role in the positioning of other membraneless organelles.

II. RESULTS

A. Birth and maturation of stress granules

To observe the dynamics of SGs throughout the cell's stress response, we perform live-imaging of human epithelial U2OS cells on a confocal microscope. Figure 1 shows representative fluorescence images of a U2OS RDG3 cell, expressing GFP-tagged G3BP1 [35], exposed to 150 μM arsenite at time zero. Let us first compare the cell before and after arsenite treatment. Figure 1(a) shows the distribution of G3BP1 at the onset of arsenite treatment and after 90 min. In accordance with previous results, we find that G3BP1 is distributed throughout the cytosol in the absence of stress but localizes in micron-sized SGs in the perinuclear region after the stress response of the cell. Formation of SGs is not the only change in the cell upon exposure to stressful conditions—the morphology of the actin network also changes. We visualize filamentous (f)-actin using SPY650-FastAct (Spyrochrome) and find that, while f-actin is initially most pronounced along the cell periphery, the actin network has significantly contracted towards the nucleus after 90 min of arsenite treatment [see Fig. 1(b)], hinting at a role for actin in directing SG motion. The full time series of the experiment is shown in Fig. 1(c) and Supplemental Movie 1 [36].

SGs appear to move rapidly towards the cell center within a few minutes after formation. Throughout this motion, SGs coalesce, leading to fewer and larger granules closer to the cell center after about 30 min of exposure to arsenite. At longer times, SGs continue to move inward and fuse, albeit at an apparently slower pace, leading to little change in SG distribution and size after about 60 min. Note that a few small SGs remain under and above the cell nucleus in the center.

SGs coalesce and migrate over time, showing initially fast dynamics that slow down over time, as qualitatively observed for a single cell. To quantify these observations, we record the position and volume of granules within the confocal stack of the G3BP1 channel over time. The circles in Fig. 1 indicate the centroid of registered SGs. Figures 2(a)–2(c) show the number of SGs, N_{SG}, the mean granule volume, $\langle V \rangle$, and the total granule volume, V_{total}, for the cell shown in Fig. 1. For the time axis, we introduce t_{SG}, which indicates the time at which the first SGs are detected in the cell. For this cell, $t_{\mathrm{SG}} = 0$ corresponds to 7.5 min after onset of arsenite treatment.

This quantification highlights three phases of SG maturation; see Fig. 2. The first phase, which we call nucleation and growth (labeled in red), lasts for about 5 min after the first SGs appear and is characterized by a rapid increase in N_{SG}, $\langle V \rangle$, and V_{total}. In the second phase, which we call fast-ripening (labeled in green), V_{total} is stable, indicating that further changes in the number and volume of SGs are dominated by ripening processes, not by further recruitment of molecules to SGs. Throughout the fast-ripening phase, we find a rapid decrease of N_{SG} that coincides with a quick increase in $\langle V \rangle$, indicative of coalescence. After about $t_{\mathrm{SG}} = 15$ min, SGs enter a slow-ripening phase, during which N_{SG} continues to decrease at a slower rate and $\langle V \rangle$ slowly increases.

To rigorously quantify this stochastic process, we combine experiments across $N = 35$ cells. Note that the duration of stress after which SGs form varies between cells, with a mean duration of 7.48 min and a standard deviation of 2.74 min. A histogram of the time after arsenite treatment at which the first SGs are detected in U2OS RDG3 is shown in Supplemental Fig. S1 [36]. Further, SGs form a bit slower in U2OS wild-type cells, with SGs appearing typically within 10–20 min after arsenite stress, suggesting that overexpression of G3BP1 and/or tagging with GFP impact the phase separation dynamics. To enable meaningful data-pooling across different cells, all cells are plated on a coverslip with fibronectin-coated patterns in the shape of a rectangle with two semicircular caps [37]. Spatially aligning micrographs of multiple cells and averaging the intensity of a given channel, we can consolidate data from live cell experiments and construct time-resolved ensemble averages, as shown in Supplemental Fig. S2 and Supplemental Movie 2 [36]. These averaged images show that the overall spatiotemporal dynamics of SG birth and maturation are highly reproducible. Ensemble averages calculated across cells fixed at distinct times after arsenite treatment reveal the same behavior; see Supplemental Fig. S3 [36].

Next, we detect SGs in each cell and pool the results for all 35 cells in Figs. 2(d)–2(f). The previously described stages (nucleation and growth, fast-ripening, and slow-ripening) remain distinct in the ensemble-averaged data, but with slightly different timing. On average, the nucleation and growth regime persists for about 5 min after formation of the first SGs. This is followed by a fast-ripening regime dominated by coalescence that lasts until about $t_{\mathrm{SG}} = 25$ min. Afterwards, SGs ripen slowly, decreasing in number and increasing in size. Ultimately, stress granules occupy about 6% of the cytoplasm. Figures 2(d)–2(f), but without introduction of the reference time t_{SG}, i.e., where time zero corresponds to the addition of arsenite to the cell media in all experiments, are shown in Supplemental Fig. S4 [36].

The distributions of SG size and shape provide further insights into their growth and maturation. Figure 2(g) shows the probability distribution of the granule volume V for 1645

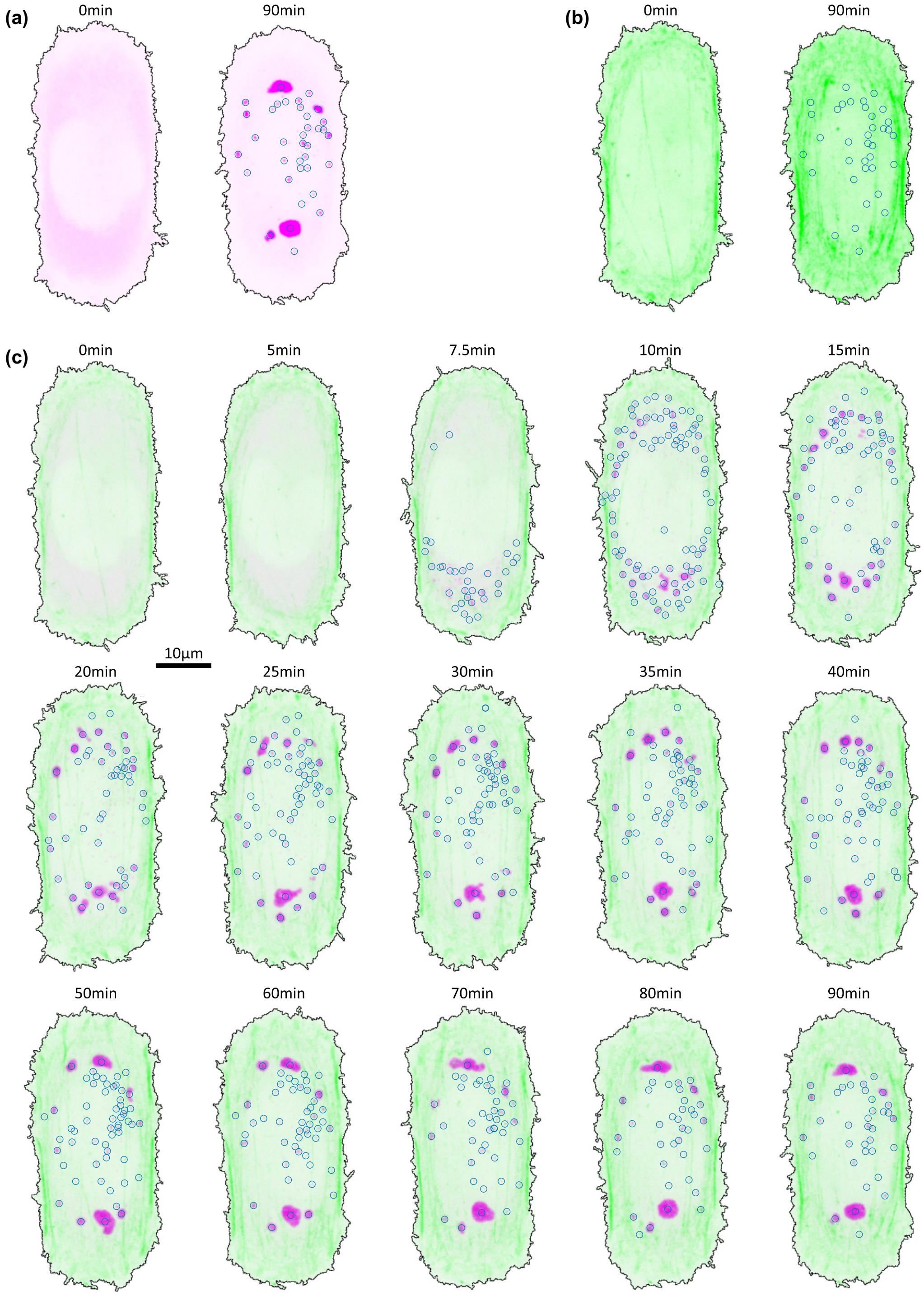

FIG. 1. Stress granule dynamics in an exemplary experiment with a U2OS RDG3 cell exposed to 150 µM arsenite at 0 min. Images show the maximum projection of a confocal stack. Color saturation is consistent within cells of a given panel. G3BP1 is shown in magenta, f-actin in green. (a) Comparison of G3BP1 at the onset of arsenite treatment and after 90 min. The blue circles indicate the position of detected SGs. The black line indicates the cell outline. (b) Comparison of actin at the onset of arsenite treatment and after 90 min. (c) Time series of an exemplary experiment. First SGs appear after 7.5 min of arsenite treatment. These images are single time-points from Supplemental Movie 1 [36].

granules at $t_{\mathrm{SG}} = 25$ min. We find that the volume distribution is consistent with a truncated power-law distribution with an exponent of about −1.5, as reported for the volume distribution of condensates in the cell nucleus [38,39].

SGs are typically not spherical. To quantify this, we calculate the principal axis (PA) ratio, i.e., the ratio of the lengths of the major and minor principal axes of an ellipse fitted to each granule. The distribution of the PA ratio at $t_{\mathrm{SG}} = 25$ min, shown in Fig. 2(h), reveals that only about 6% of all SGs are spherical. Most granules are slightly deformed and have a PA ratio between 1 and 1.5. The remaining 19% of SGs have a PA ratio larger than 1.5, reaching values beyond 4. Further,

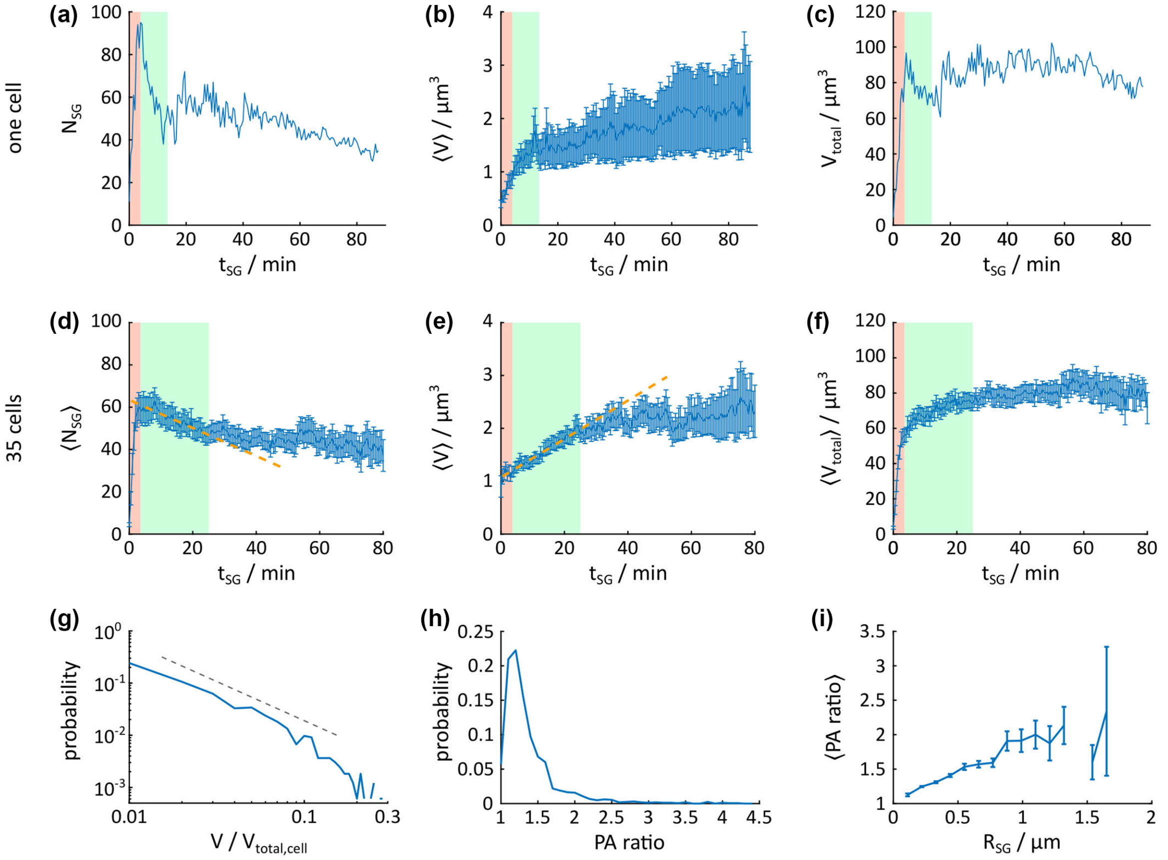

FIG. 2. Statistics of SG formation over time after detection of first granules at $t_{SG} = 0$ min. (a) The number N_{SG} of detected SGs in the cell shown in Fig. 1. (b) The average volume $\langle V \rangle$ of SGs in this cell; the error is given as the standard error. (c) The total volume V_{total} of SGs in this cell. The nucleation and growth phase is shaded in red, and the fast-ripening regime is shaded in green. (d) $\langle N_{SG} \rangle$ averaged over $N = 35$ cells; the error is given as the standard error. The orange dashed line is a guide to the eye. (e) $\langle V \rangle$ averaged over $N = 35$ cells; the error is given as the standard error. (f) $\langle V_{total} \rangle$ averaged over $N = 35$ cells; the error is given as the standard error. The red shaded area indicates the nucleation and growth regime, the green shaded area the fast-ripening regime. (g) Probability distribution of the SG volume V at $t_{SG} = 25$ min with 1645 SGs considered. V is normalized by V_{total} for each cell. The dashed line indicates a slope of -1.5. (h) Probability distribution of the principal axis (PA) ratio for the same granules at $t_{SG} = 25$ min. (i) Mean PA ratio, as a function of granule radius R_{SG} at the same time point. Error bars indicate the standard error.

the mean PA ratio increases with SG size; see Fig. 2(i). These deformations can relax over time and are thus not indicative of changes in SG material properties due to hardening (see Supplemental Movie 1 [36]), in line with previous work, which showed that SGs retain roughly constant fluidity for at least two hours after onset of stress [40]. Changes in material properties over time have, however, been observed for different protein condensates, typically on timescales of hours [41], or for SGs in the absence of ATP [9]. Since SGs are deformed from the spherical shape favored by surface tension, additional forces must be acting upon them. Consistent with this, previous results have revealed structural correlations between the cytoskeleton and nonspherical SGs [31].

B. Interactions of stress granules with microtubules and actin

The cytoskeleton is a complex network spanning the cytoplasm composed of actin, microtubules, and various intermediate filaments. The cytoskeleton has heterogeneous material properties [24]—its organization and mesh-size vary throughout the cytoplasm [42,43].

SGs interact with microtubules, as found in previous studies. While early studies suggested that the observed colocalization of SGs was related to motor proteins [25–29], recent work has highlighted the importance of wetting interactions between microtubules and SGs that lead to a significant enhancement of microtubule density around SGs. These wetting interactions are a consequence of SGs' native surface tension. Tubulin dimers, the molecular building blocks of microtubules, have no preference to be either inside a SG or in the cytosol. Consequently, tubulin acts as a weak Pickering agent, adsorbing to the SG interface and lowering its surface energy. While the adhesion strength of isolated tubulin dimers is less than k_BT, i.e., the energy associated with thermal fluctuations, polymerized microtubules can bind strongly, with an adhesion strength per contact length of up to $50k_BT/\mu$m, leading to nonspecific adhesion of microtubules to SGs, rendering microtubule-rich regions of the cell energetically favorable for SGs [31].

Building upon these findings, we compare the interactions of SGs with microtubules and f-actin. We take a structural approach, quantifying the correlations of SGs with actin and

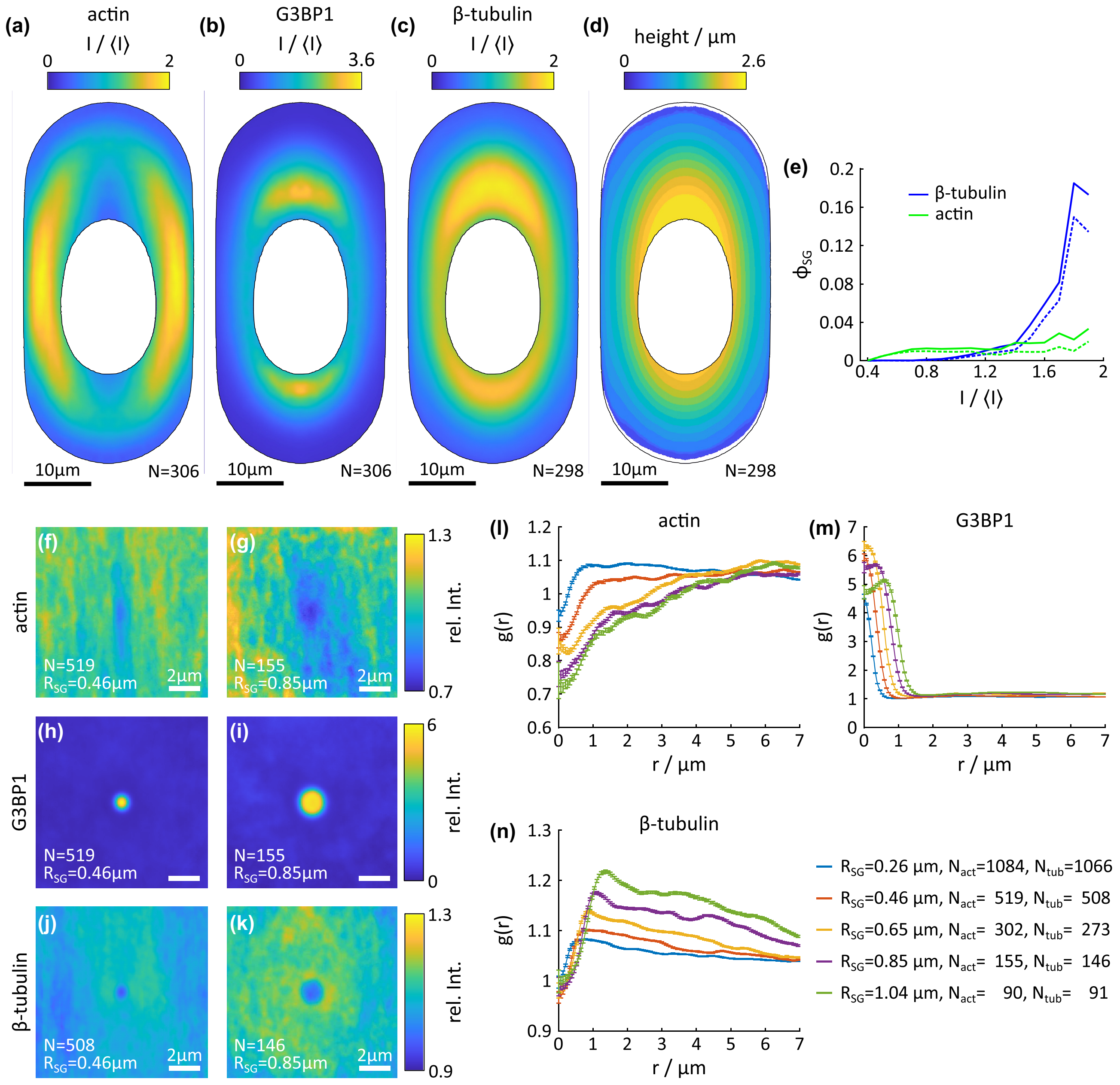

FIG. 3. Stress granules are attracted by microtubules and effectively repelled by actin. (a)–(c) One xy-slice of the reference cells of actin, G3BP1, and β-tubulin averaged over N cells fixed after 90 min of exposure to arsenite. We show the xy-slice corresponding to the highest intensity in both actin and β-tubulin. Intensity is normalized by the average intensity in each individual cell and channel $\langle I\rangle$. The black line indicates the extent of the cytoplasm around the nucleus in the center. (d) Height profile of the reference cell. (e) Conditional volume fraction $\phi_{\mathrm{SG}}(I/\langle I\rangle)$ of stress granules in regions of the reference cell with a given intensity of the actin and β-tubulin channel. Solid lines indicate ϕ_{SG} calculated based on the detected SG volume, while dashed lines show ϕ_{SG} calculated assuming a spherical granule with a radius given by the location of the maximum gradient across the interface of individual SGs. (f)–(k) Two sets of distribution maps of actin (f),(g), G3BP1 (h),(i), and β-tubulin (j),(k) for roughly spherical SGs (principal axis ratio below 1.5) with a radius in the interval from 0.39 to 0.52 μm (indicated as $R_{\mathrm{SG}} = 0.46$ μm) and from 0.78 to 0.91 μm (indicated as $R_{\mathrm{SG}} = 0.85$ μm). N gives the number of contributing images. (l) Radial distribution function $g(r)$ of actin for SGs of varying size. (m),(n) $g(r)$ for G3BP1 and β-tubulin, respectively. The controls for the data in panels (f)–(n) are shown in Supplemental Fig. S7 [36].

microtubules, using confocal stacks of wild-type U2OS cells fixed after 90 min of exposure to arsenite. All cells are plated on the same patterned substrate and can therefore be spatially registered and aligned. Averaging over about 300 cells, we construct *reference cells* that capture the typical distribution of f-actin, β-tubulin, and G3BP1 in these cells; see Figs. 3(a)–3(c). Note that reference cells are fully resolved in three dimensions; see Supplemental Fig. S5 [36]. For comparison, an example of the actin, SG, and β-tubulin channels for a single cell is shown in Supplemental Figs. S6(a) and S6(b) [36]. Reference cells are given in units of $I/\langle I\rangle$, where $\langle I\rangle$ is the average intensity per cell. The nucleus, as well as the volume above and below it, are masked based on a DAPI stain. For detailed information on the construction of the reference cells, refer to the Materials and Methods section and [31]. We find that the actin and microtubule networks are dense in different regions of the cell, with microtubules predominantly in the perinuclear region of the cell and actin on the periphery. The high intensity of G3BP1 tends to colocalize with high β-tubulin intensity, while actin-rich regions show a low G3BP1 signal. A similar observation is made when directly correlating the local intensity of G3BP1 with actin and β-tubulin intensity before and after arsenite treatment, showing that SGs tend to grow in microtubule-rich and actin-low regions of the cell; see Supplemental Figs. S6(c) and S6(d) [36].

Actin-rich regions in the cell periphery are lower in height than the region around the cell nucleus, where most microtubules are located. The apparent affinity of SGs towards microtubules and avoidance of actin might therefore be impacted by volume effects. To probe for such effects, we quantify the cell height through a low-intensity threshold of the β-tubulin channel as shown in Fig. 3(d). We find that the cell height continuously increases from the cell periphery towards the cell nucleus. The maximum of G3BP1 intensity, however, coincides with the highest intensity in the microtubule network and not with the regions of largest cell height. Further, side views of the reference cells, shown in Supplemental Fig. S5 [36], reveal that the colocalization of G3BP1, and β-tubulin also holds across the height of the cell. These observations rule out local cell height as the main driving force for the positioning of SGs.

To probe the affinity of SGs to actin and β-tubulin, we introduce the conditional volume fraction $\phi_{\mathrm{SG}}(I/\langle I\rangle)$. $\phi_{\mathrm{SG}}(I/\langle I\rangle)$ is calculated as the volume of stress granules within a region of given $I/\langle I\rangle$ of the reference cell for β-tubulin or actin, divided by the volume of this region of the reference cell and the number of contributing cells; see Materials and Methods and Fig. 3(e). We find that, at very low $I/\langle I\rangle$ of actin, i.e., at the very cell edge, no SGs are present. Regions of intermediate actin intensity have a roughly constant ϕ_{SG} of about 0.02, which only increases slightly to about 0.03 in regions of high actin intensity. For β-tubulin, we find a very different behavior. ϕ_{SG} increases with increasing tubulin intensity, reaching surprisingly high values of about 0.16 in the regions of highest β-tubulin intensity, suggesting a strong affinity of SGs for microtubule-rich regions. We conclude that SGs have a strong tendency to colocalize with β-tubulin-rich regions of the cell and tend to avoid the actin-rich cell periphery. Note that the volume fraction in fixed wild-type U2OS is not immediately comparable to measurements in live cell experiments with U2OS RDG3 due to the overexpression of G3BP1 and the addition of GFP as well as different SG detection routines (see Materials and Methods).

While we have broadly quantified the tendency for SGs to inhabit/avoid regions of the cell rich in microtubules/actin, the above analyses do not resolve the interactions of individual SGs with cytoskeletal filaments. To that end, we quantify local structural correlations of the microtubule and actin network around SGs. This correlation analysis leads to *distribution maps* shown in Figs. 3(f)–3(k). Distribution maps reveal the average environment of a given channel around SGs of selected size and shape, here SGs with a roughly spherical shape (having a PA ratio below 1.5) binned by their radius R_{SG} in steps of 0.195 μm. Throughout the construction, individual images contributing to distribution maps are normalized against the respective region of the reference cell; see Materials and Methods and Ref. [31]. Distribution maps consequently show average changes of the cytoskeleton in the presence of stress granules in units of *relative intensity*. A value of 1 indicates that the observed intensity is identical to the reference cell, while values above (below) 1 reveal an increase (decrease) by a factor given by the local relative intensity. A computational negative control for this analysis is shown in Supplemental Fig. S7 [36].

The distribution maps of G3BP1 for “small” (here $R_{\mathrm{SG}} = 0.46$ μm) and “large” ($R_{\mathrm{SG}} = 0.85$ μm) SGs show spherical regions of elevated G3BP1 intensity with a radius corresponding to the radius of the contributing SGs; see Figs. 3(h) and 3(i). To quantitatively compare SGs of different size, we introduce the *radial distribution function* $g(r)$, essentially the azimuthal average of the distribution map. For details on the calculation, refer to Materials and Methods and Ref. [31]. $g(r)$ for G3BP1 is shown in Fig. 3(m) and shows the expected outward shift for the granule interface from high to low intensity as R_{SG} increases. A close look at $g(r)$ for G3BP1 reveals that G3BP1 is enhanced in the vicinity of SGs; see Supplemental Fig. S8 [36]. This enhancement increases from about 1.1 around small SGs to values between 1.2 and 1.3 as R_{SG} increases. Directly around SGs, we find a dip in G3BP1 intensity that does not, however, fall below a relative intensity of 1. This suggests that SGs are more likely to be found in regions with more G3BP1 compared to the reference cell.

This correlation analysis further reveals different affinities of SGs towards actin and microtubules. Distribution maps of actin around small SGs show that actin retains its normal configuration, i.e., a stripelike morphology originating from stress fibers, around such small SGs [Fig. 3(f)]. SGs expel or avoid actin fibers, since the relative intensity of actin throughout the granule itself is below 1. For larger SGs, this depletion of actin extends well beyond the granule radius; see Fig. 3(g). $g(r)$ for actin, shown in Fig. 3(l), clearly shows the emergence of a zone of depleted actin intensity around larger SGs, extending over 3 μm around the largest SGs. Interestingly, the smallest SGs are found to have a higher than expected actin intensity around them, suggesting that high local actin intensity hinders granule growth.

For the microtubule channel, on the other hand, we find a tubulin intensity close to 1 inside the granule and an enhancement in β-tubulin intensity in the immediate vicinity of SGs of all sizes. This enhancement is centered on SGs and increases in magnitude as SG size increases [Figs. 3(j) and 3(k)]. Further, it decays roughly linearly as the distance from the granule increases, extending over several granule radii around SG. These observations are particularly clearly visible in $g(r)$ [Fig. 3(n)]. We previously interpreted these observations with adhesive capillary forces between SGs and microtubules [31]. Interestingly, the extent of the enhancement in β-tubulin intensity around larger SGs corresponds roughly to the depletion zone in the $g(r)$ for actin. This suggests steric repulsion between f-actin and microtubules.

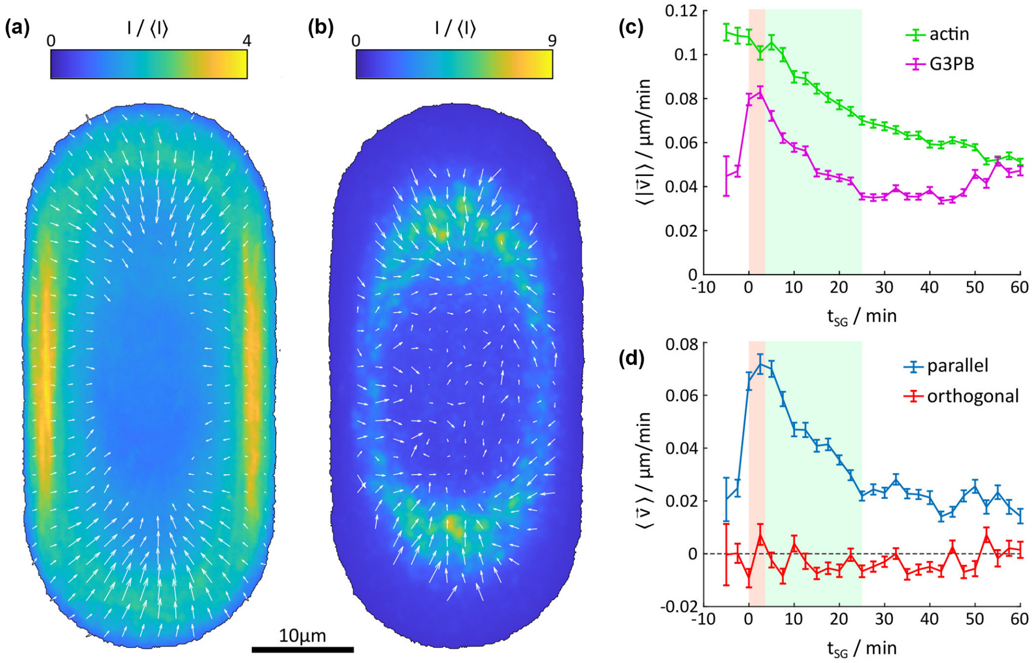

FIG. 4. Actin and G3BP1 flow are aligned. (a) PIV ensemble for $t_{\mathrm{SG}} = 10\,\mathrm{min}$ for the actin channel overlain with the actin ensemble-average over the same data. (b) The corresponding PIV ensemble for G3BP1. (c) The mean speed of actin and G3BP1 throughout the cell over time. Error bars show standard error. The nucleation and growth and fast-ripening regime are shaded in red and green (compare Fig. 2). (d) Spatially averaged velocity of SGs parallel and orthogonal to local actin flow. Parallel movement along local actin flow is positive; orthogonal flow is positive towards the left relative to local actin flow. Error bars show standard error.

Overall, these results show that SGs exclude f-actin from within their volume and that larger SGs have less actin around them. For microtubules, we find an affinity to the SG interface consistent with capillary adhesive interactions between SGs and microtubules. This static correlation analysis is informative of interactions between SGs and cytoskeletal filaments. To visualize how these interactions could ultimately determine the position of stress granules, however, we next return to live cell experiments.

C. Time-resolved transport of stress granules

While SGs form throughout the cytoplasm, they are strongly localized to the perinuclear, microtubule-rich region after about $t_{\mathrm{SG}} = 25\,\mathrm{min}$. This shift in SG distribution toward the perinuclear region occurs primarily during their nucleation and growth and fast-ripening phases, as seen in the exemplary cell (Fig. 1) as well as in time-resolved reference cells from live-cell experiments (Supplemental Fig. S2 [36]) and reference cells constructed from cells fixed after varying time of arsenite treatment (Supplemental Fig. S3 [36]). The inward transport of SGs is reminiscent of retrograde flow of actin in the lamellopodium [43,44].

To investigate a potential coupling of SG-transport with flow of the actin network, we performed particle image velocimetry (PIV) of actin and G3BP1. To quantify the average flow speed and direction of both f-actin and G3BP1, we construct *PIV ensembles*, by averaging PIV results from individual cells over time bins of 2.5 min and, again, averaging these results over 35 cells. For details on the PIV analysis, refer to Materials and Methods. Figures 4(a) and 4(b) show the PIV ensembles for the actin and G3BP1 channels at $t_{\mathrm{SG}} = 10\,\mathrm{min}$. The full time series of PIV ensembles is shown in Supplemental Movie 3 [36]. We find that actin flow is directed towards the cell center and is especially pronounced in the lamellar regions at the curved ends of the cell. The flow of G3BP1 is also, on average, inward but exhibits larger fluctuations.

The cell-wide average speeds, $|\vec{v}|$, of actin and G3BP1 over time are shown in Fig. 4(c). The average actin speed is initially steady at about $0.11\ \mu\mathrm{m/min}$. At the same time, the maximum speed is higher, reaching $0.29\ \mu\mathrm{m/min}$; see Supplemental Fig. S9(a) [36]. These values are consistent with previous reports of actin flow rates [44,45]. As the cell responds to stress, actin flow continuously slows down. The observed actin flow has two contributions, namely lamellar retrograde flow [44,45] and a stress-induced net contraction of the actin cytoskeleton, which leads to ingress of actin towards the perinuclear region [46]. The latter is most clearly visible by comparing the actin reference cells across time; see Supplemental Figs. S2 and S3 [36]. Plotting the intensity distribution of actin along the long axis of symmetry of the reference cells, we find a contraction speed of about $0.1\ \mu\mathrm{m/min}$ along this center line; see Supplemental Fig. S10 [36]. Contraction occurs symmetrically on both sides of the nucleus at a roughly constant speed from $t_{\mathrm{SG}} = 0$ to about 40 min, then fully stops after about $t_{\mathrm{SG}} = 50\,\mathrm{min}$, during the slow-ripening phase, suggesting that the slow-down of actin flow at earlier times is caused by a slow-down of retrograde flow; see also Supplemental Fig. S9(a) [36].

SGs are the fastest throughout the nucleation phase, with the cell-wide average of the G3BP1 channel reaching

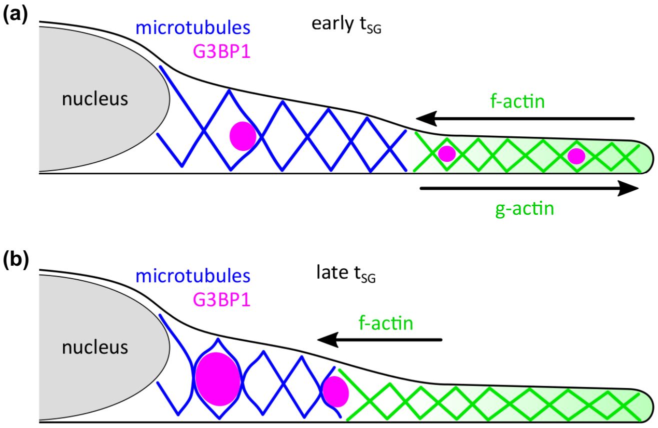

FIG. 5. Model of the interactions between stress granules, f-actin, and microtubules. (a) Right after nucleation and growth of SGs, SGs in the lamellar region are subject to retrograde flow of f-actin and move towards the cell center, where they are handed over to the microtubule network. After the nucleation and growth phase, SGs grow predominantly through coalescence. (b) At longer times, f-actin contracts, leading to further inward flux of SGs and f-actin. Favorable wetting interactions between microtubules and SGs lead to mutual deformations of SGs and the microtubule network, as well as stable positioning of SGs in the microtubule-rich perinuclear region.

0.08 μm/min, and a maximum speed of 0.25 μm/min [Supplemental Fig. S9(b) [36]]. The average SG speed then decays to about 0.04 μm/min during the fast-ripening regime, after which it stays roughly constant at about 0.04–0.05 μm/min. Note that the increase in speed at very late times is affected by increasing skew in the size distribution, with few large SGs and small ones, often above or below the nucleus.

To quantify the alignment of SGs to actin flow, we decompose the local SG velocity into components parallel and orthogonal to local actin flow; see Fig. 4(d). We find that the parallel component remains positive, i.e., aligned to actin flow, at all times. SG flow in the direction of actin flow shows the highest flow speeds throughout the nucleation phase, slows down throughout the fast-ripening phase, and finally reaches a roughly constant speed of around 0.2 μm/min in the slow-ripening regime. Note that SGs are, at all times, slower than the actin flow, suggesting slip or viscoelastic effects. The orthogonal velocity component fluctuates around zero at all times, suggesting that motion orthogonal to actin flow is random. Our data suggest that retrograde flow of actin leads to rapid transport of SGs out of the lamellar region of the cell and that subsequent contraction of the actin network induces further inward displacement of SGs. These results are consistent with an alternative analysis based on tracking of SGs and actin intensity profiles presented in Supplemental Fig. S11 [36].

D. Emerging model and perturbations

Integrating the above results, the following qualitative model, illustrated in Fig. 5, emerges for the interactions of stress granules with the cytoskeleton: Upon stress, SG nucleation and growth occurs rapidly throughout the cytoplasm, and is complete within about 5 min after the appearance of the first SGs (Fig. 2). The f-actin network of the lamellae, with a mesh size on the order of 100 nm [47–49], is dense enough to confine all well-resolved stress granules. This couples SGs to actin's native retrograde flow and transports SGs into the center of the cell. Subsequent contraction of the actin network, now largely void of SGs, further guides SGs toward the cell center. Actin-driven transport thus concentrates SGs in the perinuclear region, increasing the rate of coalescence.

SGs that form in the perinuclear region, as well as those transported there by actin, interact with the microtubule network that is particularly dense in this region of the cell (see Fig. 3). SGs engage in energetically favorable wetting interactions with microtubules further driving SGs toward regions of high microtubule density and leading to mutual deformation of microtubule network and SGs [31,50].

To challenge this model, we quantify the impact of various cytoskeletal perturbations on the spatial distributions of stress granules, and their structural correlations with actin and microtubules. Cells are treated with the respective drugs for 30 min before inducing stress granules, ensuring that the desired effect upon the cytoskeleton is present at the onset of SG formation (see Materials and Methods).

First, we interrogate the importance of the microtubule network in defining the final localization of SGs. Depolymerizing the microtubule network with nocodazole [51] before the onset of stress, we find that SGs are still excluded from the actin-rich lamella region, but are dispersed throughout the perinuclear region, in line with previous results that found that SGs are smaller and more dispersed in nocodazole-treated cells [13,14]. The reference cell of G3BP1 after nocodazole treatment is shown in Fig. 6(b). This observation is in line with the proposed model: Actin transport still drives SGs toward the center of the cell. In the absence of microtubules, however, SGs do not show a pronounced localization within the perinuclear region. $g(r)$ for actin around SGs of intermediate radius ($R_{SG} = 0.65$ μm) reveals a similar expulsion of actin from the bulk of the SG in nocodazole-treated cells as in cells treated with arsenite alone. Outside SGs, however, $g(r)$ for actin assumes a constant value in nocodazole-treated cells; see Fig. 6(e). The exclusion zone of actin around SGs observed in cells treated with arsenite only is not present, suggesting that a dense microtubule network around SGs might indeed be the source of the exclusion of actin. $g(r)$ for β-tubulin, here importantly in the form of tubulin dimers, shows a distinct peak at the granule interface [Fig. 6(f)]. This is consistent with tubulin dimers acting as Pickering agents leading to weak adhesive interaction between the SG interface and microtubule subunits [31]. The full results for nocodazole-treated cells, including reference cells for all channels and correlation analyses, are shown in Supplemental Fig. S12 [36].

Next, we probe the importance of actin for concentrating SGs in the perinuclear region. Disruption of the f-actin network with jasplakinolide completely arrests actin dynamics and leads to aggregation of actin in amorphous masses around the cell nucleus [52,53]. Live-cell experiments show that after nucleation and growth, SGs in jasplakinolide-treated cells do not migrate toward the center of the cell, and display reduced coalescence; see Supplemental Movie 4 [36]. As a result, SGs remain widely distributed throughout the cell, not just within the perinuclear region, as seen in the reference cell

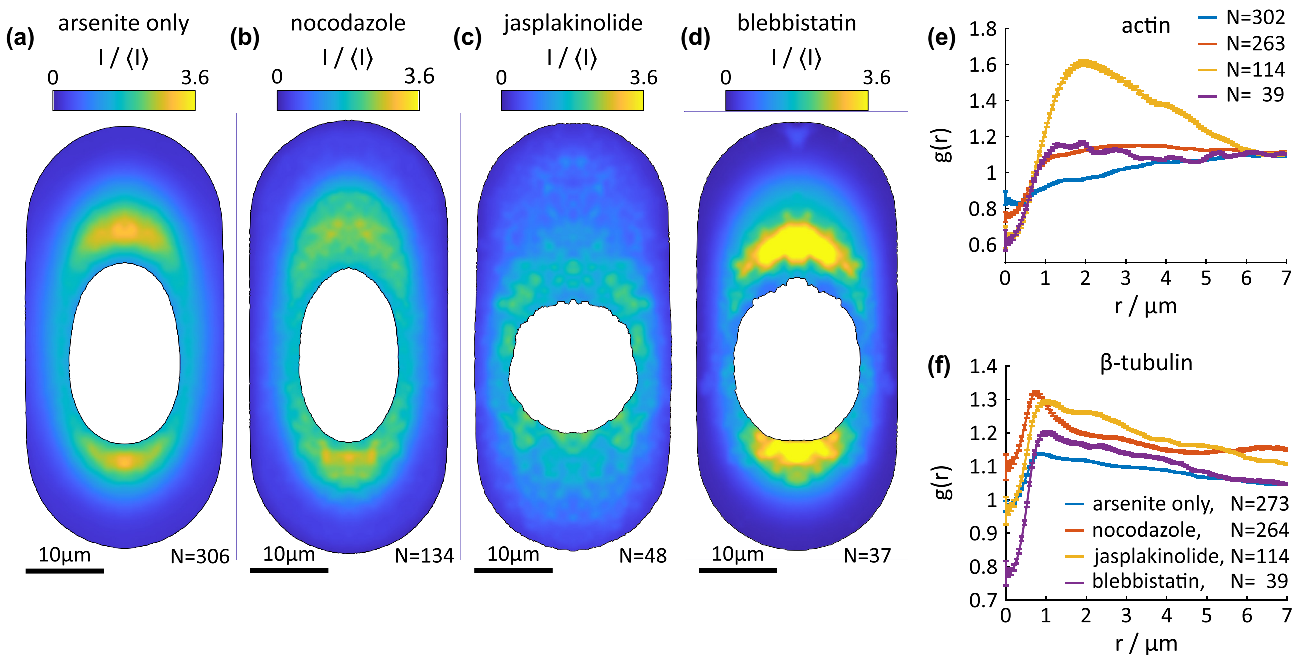

FIG. 6. Perturbing the cytoskeleton affects the positioning of stress granules. Reference cells of G3BP1 for cells treated for 90 min with arsenite only (a), treated with nocodazole before SG formation (b), treated with jasplakinolide before SG formation (c), and treated with blebbistatin before SG formation (d). Note that the colormap in panel (d) is saturated but kept identical for comparison purposes. An adjusted version can be found in Supplemental Fig. S14 [36]. $g(r)$ of actin (e) and tubulin (f) for SGs with $R_{SG} = 0.65$ µm for cells with different drug treatment.

in Fig. 6(c). Jasplakinolide seems to have a minimal effect on the interaction of SGs with microtubules, as seen by the very similar shape of $g(r)$ [Fig. 6(f)]. The magnitude of enhancement of microtubules around SGs, however, is enhanced compared to cells treated with arsenite only. For actin, we observe a distinct enhancement in the broader vicinity of SGs, outside the peak of microtubules [Fig. 6(e)]. Note, however, that the reference cell for actin and microtubules is very different in jasplakinolide-treated cells, making it difficult to compare to other cells. In particular, jasplakinolide-treated cells are very flat compared to cells treated with arsenite or other drugs, suggesting that volume effects might impact the localization of cellular structures more strongly. The full results for jasplakinolide-treated cells, including the height profile, are shown in Supplemental Fig. S13 [36]. Overall, we find that disruption of actin leads to a broader distribution of SGs throughout the entire cytoplasm and limited mobility of SGs, in line with the proposed model.

Disruption of myosin activity through treatment with blebbistatin has only a small effect on stress granules. As expected, blebbistatin treatment almost completely removes the stress-induced contraction of the actin network [see Supplemental Fig. S14(a) [36]]. Since retrograde flow is maintained, albeit at a reduced rate [44,54], SGs are still expelled from the lamellar region, and accumulate in microtubule-rich regions of the cell center [Fig. 6(d)]. Blebbistatin does not have a major impact on the distribution of microtubules around individual SGs leading to very comparable $g(r)$ with only slightly enhanced enrichment compared to cells treated with arsenite only [Fig. 6(f)]. For actin, we find that $g(r)$ is similar to nocodazole-treated cells, i.e., without the pronounced depletion zone observed in cells treated with arsenite only [Fig. 6(e)]. This suggests that contraction, i.e., ingress of actin, may be important for the formation of the actin depletion zone around SGs, e.g., by further compacting the microtubule network around SGs. The full results for blebbistatin-treated cells are shown in Supplemental Fig. S14 [36].

Overall, these perturbations of the cytoskeleton are consistent with the emerging qualitative model proposed in Fig. 5.

III. DISCUSSION

Stress granules nucleate, grow, coalescence, and coarsen in the presence of the active and heterogeneous networks of actin and microtubules. We find that the complex architecture and dynamic nature of the cytoskeleton gives rise to robust and reproducible positioning of stress granules through hydrodynamic coupling of granule motion to f-actin flow and adhesive capillary interactions with microtubules. These mechanisms lead to localization of SGs also in the absence of compositional or temperature gradients across the cell, which would impact the local thermodynamics as observed for p granules in *Caenorhabditis elegans* embryos [18,19,21].

Interactions with the cytoskeleton also affect the positioning of other protein condensates in cells. Confinement of nuclear protein condensates by static nuclear actin networks slows down gravitational creep flow in oocytes [55,56]. Dynamic actin networks, on the other hand, have been shown to drive localization of membrane-bound cell receptor condensates on the membrane of T cells [57,58]. These membrane-bound condensates may, depending on their composition, stick to actin and directly couple to actin flow or be continuously “swept” inward by passing actin filaments [58,59]. We report similar actin-driven transport in the bulk of the cytoplasm, where SGs are transported along retrograde flow and actin contraction. The observed effectively repulsive interactions between actin and SGs, as well as the fact that SG flow is slower than actin flow, suggest that SGs are also transported (or "swept") by transient association with the actin network, likely originating from steric confinement. The impact of actin flow on positioning and symmetry formation in cells has also been captured *in vitro* in a reconstituted system [60].

Positioning of cellular structures due to microtubules is typically associated with motor proteins. However, various protein condensates have been shown to wet microtubules [31,61,62], giving rise to preferential localization within the cell, as we observed for SGs. Because of the generic nature of these physical interactions, i.e., coupling to actin flow and wetting, we expect that such interactions could also play a role in the dynamics of other protein condensates. Further, modulations of a given protein condensate's material properties and wetting behavior, e.g., through phosphorylation, may enable the cell to selectively couple condensates to cytoskeletal dynamics.

These findings have been made possible by novel quantitative methods allowing us to measure physical quantities amenable to theory in the noisy system of the cell. In contrast to previous studies on SG dynamics, we employ patterned cells ensuring reproducible cell geometry and resulting morphology of the cytoskeleton. We analyze our results using statistical approaches, averaging over large data sets in order to extract ensemble averages and typical behaviors. We anticipate that these approaches can enable more quantitative analysis also in other biological systems.

From a biological perspective, we expect that the final positioning of SGs in the perinuclear region may have functional importance. SGs are dynamic sites of mRNA regulation [10,17,63], suggesting a close interplay with the cell nucleus. Indeed, a number of regulatory RNA-binding proteins have been shown to traffic between the nucleus and SGs [64–66]. Proximity of SGs to the nucleus might therefore ensure efficient signaling through short diffusion times of related proteins. Further, due to the observed effective repulsion between SGs and f-actin, the actin cortex, lining the cell membrane, may act as a barrier that inhibits interactions of cytosolic protein condensates with the cell membrane.

IV. MATERIALS AND METHODS

For more detailed Materials and Methods, also refer to Refs. [31,67].

A. Cell culture

U2OS human osteosarcoma cells are grown in Dulbecco's Modified Eagle Medium (DMEM, ThermoFischer, cat. num. 41966029) supplemented with 10% fetal bovine serum (FBS, ThermoFischer, cat. num. 10270106), and 2 mM L-glutamine (ThermoFisher, cat. num. 25030024), at 37 °C in 5% CO_2. We use both wild-type cells as well as U2OS RDG3. U2OS RDG3 have green fluorescent protein (GFP)-tagged G3BP1 to mark SGs as well as red fluorescent protein (RFP)-tagged DCP1a, a processing body protein [35,68,69]. Both cell lines were kindly supplied by the Pelkmans Lab at the University of Zurich.

B. Micropatterning

Cells are plated on patterned coverslips to ensure consistent cell shapes. The pattern consists of a 25 μm by 30 μm rectangle with two hemispherical caps with a radius of 12.5 μm, similar to the patterns used by Oakes *et al.* [37].

Patterned coverslips are fabricated using 22 mm by 22 mm glass coverslips. Coverslips are initially cleaned and rinsed with ethanol by hand and subsequently cleaned by exposure to deep ultraviolet (UV) light in a UV/ozone cleaner (ProCleaner Plus BioForce Nanosciences) for 5 min. The cleaned coverslips are then incubated in 0.1 mg/mL poly-L-lysine-g-poly(ethyleneglycol) [PLL(20)-g[3.5]-PEG(2), SuSoS AG] for 1 h and subsequently rinsed with ultrapure water.

A quartz photomask (printed by Deltamasks) containing transparent features corresponding to the desired cell pattern in an otherwise opaque chrome coating is cleaned in the same fashion as coverslips using ethanol and 5 min in a UV/ozone cleaner. One mask contains several hundred features per coverslip. Features are spaced at least 100 μm apart from edge to edge in all directions. The coated coverslips are mounted onto the photomask with the coated side in contact with the mask, using the capillary forces of a thin water film between glass and mask (about 8 μL water per coverslip). The mounted coverslips are then exposed to deep UV light through the mask in a UV/ozone cleaner for 10 min. After UV treatment, coverslips are detached by floating the coverslips with water and stored in ultrapure water for up to three weeks.

During experiment preparation, the patterned coverslips are first submerged in 70% ethanol for at least 5 min and subsequently rinsed three times with phosphate-buffered saline (PBS). Coverslips are then coated with 20 μg/mL of fibronectin (Sigma-Aldrich) for 12 min, washed with PBS, and finally washed with cell media.

C. Fixed cell experiments

1. Immunofluorescence

Cells are plated on patterned coverslips in six-well plates at a concentration of about 5×10^4 cells per well 4–6 h prior to experiments to ensure sufficient spreading. After specified durations of treatment with 0.5 mM sodium arsenite (Sigma-Aldrich) to induce stress granule formation [32], or additional drug treatment depending on the experiment, U2OS cells are fixed with 4% formaldehyde for 15 min, permeabilized with 0.1% Triton X-100 in PBS for 20 min, and blocked with 5 mg/mL bovine serum albumin (Sigma-Aldrich) for 1 h. Fixed cells are incubated with primary antibodies overnight at 4 °C. Primary antibodies are mouse anti-G3BP (1:500 in blocking solution, abcam ab56574) and rabbit anti-β-tubulin (1:200 in blocking solution, abcam ab6046). Note that G3BP does not co-precipitate with β-tubulin immunoprecipitation and is commonly used as a stress granule marker [26,69,70]. On the next day, cells are stained with secondary antibodies for 1 h at room temperature. The secondary antibodies are Rhodamin Red-X antimouse IgG (1:500 in blocking solution, Jackson ImmunoResearch, cat. num. 115-295-003) and

Alexa 647 antirabbit IgG (1:500 in blocking solution, Jackson ImmunoResearch, cat. num. 111-605-144). Actin is stained using 488 nm-phalloidin (ThermoFischer, cat. num. A12379). DNA is stained by subsequent incubation in DAPI solution (1:1000 in PBS, SigmaAldrich, cat. num. D9542-10MG) for 15 min at room temperature. Coverslips are finally mounted in ProLong Gold or Diamond (both Thermo Fisher). Cells are washed three times with PBS in between steps.

2. Fixed cell imaging

Confocal stacks of fixed cells are imaged on a Nikon Ti2 Eclipse with a Yokogawa CSU-W1 spinning disk and 3i 3iL35 Laser Stack using a 100× oil objective with a numerical aperture of 1.45 and a Hamamatsu Orca-flash 4.0 camera. The spatial resolution in the focal (xy-)plane is 0.065 μm/pixel and the step height (z-direction) is 0.2 μm.

The theoretical diffraction limit for the longest used wavelength (640 nm), here defined as the full width at half-maximum of the theoretical point spread function of a confocal microscope, is 160 nm, calculated as $\frac{0.51\lambda}{\sqrt{2}NA}$ with numerical aperture NA [71]. For the actual optical setup, we assume a diffraction limit of three pixels (corresponding to 195 nm).

3. Cell detection and sorting

Image analysis is carried out using MATLAB and is largely automated to allow for efficient and reproducible processing of a large number of cells. The protocol outlined below is used for fixed cells, but the data processing of live-cell experiments is largely analogous. Each set of confocal data acquired on the microscope contains one cell. The cell is identified in the xy-plane using the *regionprops* function on an overlay of the maximum projections along z of all channels as well as a wide-field image of the nucleus through the DAPI stain. For the accurate detection of the cell shape in the focal plane, the image is sharpened before thresholding. All images are cropped around the detected cell in the xy-plane. To determine the z-coordinate of the base of each cell (cell base height), we calculate the sum of the median and 80th percentile for each xy-plane of the cytoskeleton channel. With only a small rim of background around the cropped cells, the median of the image is slightly below the median intensity of the cell and serves as a proxy for the overall structure of the cell. The 80th percentile captures more pronounced features, such as individual filaments, while being robust against outliers. The cell base height is then determined as the z-coordinate corresponding to the maximal gradient of this intensity measure, which detects reliably the side of the cell attached to the coverslip. We assume an error of this measurement of ± 1 z-step. The maximum intensity z-slice is then typically two to four slices above the cell base height. Cells in which this distance falls outside of this interval are discarded. Moreover, cells with an area outside 85–110 % of the area of the prescribed pattern (1257 μm^2) are discarded. Cells with a ratio of the short principal axis to the long principal axis outside the interval [0.43 0.55] are also discarded. The corresponding ratio of the pattern itself is 0.45. These criteria have been chosen based on the corresponding histograms of all cells to discard outliers.

The background intensity of each channel is approximated from the intensity in the corners of the cropped image outside the detected cell. Each channel is corrected for this background intensity individually.

Multiple cells are recorded on each coverslip in one acquisition session. Within one such batch, all patterns have the same orientation. The orientation of the patterns is determined as the mean orientation of cells from one batch. Batches with fewer than 10 cells remaining after filtering the cell area and shape are discarded. Individual cells with an orientation that deviates by more than 3° relative to the pattern orientation are also discarded. All cells are then rotated by the pattern orientation to ensure consistent cell orientation across samples. The remaining cells are aligned such that the centroid of each cell is in the center of the xy-plane. Because the nucleus is typically not exactly in the center of the cell, some cells are rotated by 180° such that the centroid of the nucleus always falls in the same side of the image.

4. Intensity normalization

The intensities of the G3BP1, actin, and β-tubulin channels of each cell are individually normalized by their respective mean intensity $\langle I \rangle$ to account for differences in protein expression, imaging, or staining. To define this mean intensity, we select a set of representative voxels. The x- and y-coordinates of representative voxels are those that fall inside the cell shape but outside the cell nucleus, based on the maximum projection along the z-coordinate of all channels. Voxels outside the cell or inside the nucleus are set to *NaN* (not a number) throughout all following analyses to ensure correct statistics. The z-positions of the representative voxels are chosen to be the second to fourth z-coordinate above the detected cell base height. Typically, the third z-coordinate above the cell base is the maximum intensity z-plane. The mean intensity for a given channel is calculated as the mean across all representative pixels. Each channel is then normalized by the respective mean intensity.

5. Stress granule detection

SGs are detected in confocal stacks of the G3BP1 channel. We determine the background by blurring the image stack with a box-kernel of a size larger than typical granules. This background is subtracted from the confocal stack. The background-adjusted image stack is then blurred with a Gaussian kernel with $\sigma = 1$ pixel in the xy-plane to decrease shot noise. The resulting filtered stack is then rescaled such that intensity values are positive by adding the minimum intensity value in a stack to each voxel.

Next, 101 threshold values evenly spaced between the maximum mean intensity value within any z-slice of the image stack and the global maximum intensity are probed to detect a suitable threshold for each cell individually. For each threshold value, entities above threshold are detected using the MATLAB function *regionprops3*, recording the position, volume, voxel list, mean, and median intensity for each connected group of voxels. With this information, we assign a quality factor to each threshold value. The quality factor is defined as the sum of the median intensity and the mean intensity across all detected particles for a given threshold value divided by the threshold value itself. The median intensity as a function of threshold level is smoothed using a running average to decrease noise. By definition, this factor is larger than or equal to 2. Too low thresholds are penalized as they pick up the surrounding of a bright region of pixels yielding low mean and median intensity, while too high thresholds are penalized by dividing by a high threshold value. Consequently, this measure approaches a value of 2 for too low as well as too high thresholds. The threshold maximizing this quality factor is taken. Cells where the global maximum is not well defined against other local maxima, i.e., here at least 7.5% higher, are discarded. All detected granules are subject to further tests. In fixed cell data, all detected entities are inflated by dilation with a sphere of three pixels radius. Particles that fuse upon dilation are discarded to ensure a minimal distance between granules. Further, SGs where the voxels, by which the granule grew upon dilation, are brighter than 55% of the intensity of the detected granule are also discarded to ensure sufficient contrast against the local environment. In the fixed cell data, granules, typically very small, that reside below or above the cell nucleus, are discarded as they fall outside the cell mask.

We define the granule radius as $R_{\mathrm{SG}} = \sqrt{A_{\mathrm{SG}}/\pi}$, where A_{SG} is the area of the stress granule projected into the xy-plane. To identify the physical interface of SGs, we correct R_{SG} using an intensity profile calculated as a function of distance to the initially detected SG interface (this quantity is called $g_s(d)$ in previous work [31,67]). R_{SG} is then corrected to align with the maximum gradient of this G3BP1 intensity profile. SGs where the maximal gradient across the interface is further away than 2 pixels from the initially detected interface are discarded. For live-cell experiments, R_{SG} is, on average, shifted by -0.34 ± 0.69 pixel, with errors given as the standard deviation. For fixed cell experiments, the average position of the maximal G3BP1 gradient is at -0.84 ± 0.65 pixel relative to the interface based on thresholding alone, i.e., we slightly overestimate granule size with the initial SG detection. Granules with a radius below the optical resolution limit are discarded; see Materials and Methods, Sec. IV C 2.

Aside from the characteristics (position, orientation, volume, etc.), a number of images are saved for each granule. All images are centered on the centroid of a given granule and show the xy-plane closest to the granule centroid. Note that pixels within these images that fall outside the cytoplasm are set to *NaN*. Note that the mask for fixed cells also excludes the nucleus, while the mask in live cell data only defines the cell edge. The size of extracted images is about 14 × 14 μm, sufficient to capture also the long-range deformations of the cytoskeleton around granules.

6. Construction of the reference cell

The alignment of all cells in three dimensions allows us to construct cell stacks by averaging over all cells that belong to the same experimental conditions, e.g., duration of arsenite treatment or drug treatment. Each individual cell stack is blurred in the xy-plane using a Gaussian kernel with a variance of 4 pixels. While this method retains the overall intensity, noise as well as single filaments are blurred to suppress short-range fluctuations. To capture the finite size of the cytoplasm as well as of the nucleus, each cell is masked by the cell outline and the nucleus shape. Based on these stacks, the reference intensity for any spatial coordinate is calculated as the mean intensity across all cells at this position, omitting the data from cells where the given pixel is masked. If more than half of the intensity values for a given coordinate fall within the masks of the nucleus or cell outline, the pixel is considered outside the cytoplasm of the reference cell. This way, the reference cell also serves as a mask for the expected cell shape.

The symmetry along the short axis of the cell has deliberately been broken during cell alignment by rotating all cells such that the cell nucleus falls into the same half of the cell. The remaining symmetry of the pattern allows to fold the cell along the center line of the long axis to enhance the statistics for the calculation of the reference cell. Using N cells, this process yields $2N$ intensity values for all spatial coordinates in one-half of the cell. The full reference cell is then recovered by mirroring the result along the center line.

Note that, due to fluctuations in the height of the cells, we only considered the intensity values between the cell base height up to 1.2 μm (six slices) into the cell as reliable. Stress granules outside this range are not considered in the following analysis.

7. Correlation analysis

Correlation analysis has been used in the cell, e.g., to study protein distributions in the lipid membrane [72,73]. The main difference here is that we account for the finite cell shape and heterogeneous cell architecture; see also Refs. [31,67].

We mainly use two analytic tools, namely the radial distribution function $g(r)$ and *distribution maps*. To calculate distribution maps, we first define a subset of SGs with comparable size and ellipticity. Images of actin, β-tubulin, and G3BP1 corresponding to round granules (i.e., with a principal axis ratio not exceeding 1.5) are binned by the granule radius R_{SG} in steps of three pixels (195 nm). Given a minimal granule radius of 195 nm, the first sized bin is [195 nm 325 nm]. This sized bin is then labeled as $R_{\mathrm{SG}} = 0.26$ μm. Each image of a given channel is then normalized pointwise by the image of the same location of the respective reference cell. All normalized images from a given channel and bin are then averaged. Note that we omit pixels that fall outside the cytoplasm of the corresponding cell, i.e., those set to *NaN*. Consequently, different pixels of a distribution map may not have the same number of pixels that contributed to the calculation of the corresponding intensity value.

Fluctuations in the number of contributing data sets for different pixel locations introduce a nonlinearity when further analyzing distribution maps, which has to be taken into account when calculating the radial distribution $g(r)$ of a distribution map. To capture the varying statistical weight, we do not take the radial average of the distribution map in question. Rather, we take the average over all intensity values that were considered for the calculation of the distribution map at a distance r from the center of the image. This way we consider the correct number of data points contributing to each entry in $g(r)$. The error of $g(r)$ at a given distance r is then calculated as the standard error, i.e., the standard deviation of the contributing values divided by the square root of the number of contributing values.

To validate the distribution maps, we perform a negative control where we extract the images corresponding to a detected SG not from the cell in which the granule was detected, but from a different cell that has been exposed to the same conditions. If all cells are listed in a table, we essentially shift the entries in this cell listing by one position, i.e., matching SGs with a different cell. This method yields random, yet biologically plausible, input that is normalized by the exact same segment of the reference cell. These negative control distribution maps, and the corresponding $g(r)$, should ideally assume a uniform value of 1.

8. Calculation of conditional stress granule volume fraction

To determine the probability of finding SGs in regions of a certain actin or β-tubulin intensity in the cell, we first assign an intensity value $I/\langle I\rangle$ to each SG that is determined by the intensity of the voxel in the three-dimensional reference cell of either actin or tubulin that corresponds to the centroid of the respective granule. With N_{SG} granules with a given $I/\langle I\rangle$, the conditional volume fraction of SGs $[\phi_{\mathrm{SG}}(I/\langle I\rangle)]$ for this intensity value is calculated as the sum over the number of voxels of SGs with this intensity value (n_{SG}) divided by the number of voxels with that $I/\langle I\rangle$ of the reference cells (n_I) and normalizing by the number of cells (N):

$$\phi_{\mathrm{SG}}\left(\frac{I}{\langle I\rangle}\right)=\frac{\sum_i^{N_{\mathrm{SG}}} n_{\mathrm{SG},i}}{n_I N}.$$

Note that n_I is calculated based on the three-dimensional information of the reference cells. This calculation of ϕ_{SG} is based on the volumetric extent of each SG as determined by the SG detection routine. These values, however, typically overestimate granule volume as the maximum gradient in the intensity profile of G3BP1 across the granule interface is observed to often fall inside the detected granule outline (see Materials and Methods, Sec. IV C 5). While the error is minimal for live-cell data (−0.3 pixel on average), we observe that the maximum gradient is typically at a distance of −0.8 pixel in fixed cell data, which are used for this analysis. While R_{SG} can readily be corrected to align with the position of the maximum gradient in intensity of G3BP1 across the granule interface, correcting the number of voxels n_{SG} accordingly is not so easy due to several caveats, such as a noncubic size of voxels due to differences in resolution in xy and z. To estimate the error of the volume fraction, we employ a second method to calculate ϕ_{SG}. Here, we consider the corrected R_{SG} in the xy-plane of each granule and assume a spherical granule shape:

$$\phi_{\mathrm{SG}}\left(\frac{I}{\langle I\rangle}\right)=\frac{\sum_i^{N_{\mathrm{SG}}} \frac{4\pi}{3} R_{\mathrm{SG},i}^3}{n_I N\cdot V_{\mathrm{voxel}}},$$

with volume per voxel V_{voxel}. This method assumes a spherical shape and thus likely underestimates the granule volume in many instances. Indeed, ϕ_{SG} calculated based on the corrected R_{SG} typically yields values below ϕ_{SG} based on the detected SG volume. For irregular shapes, in particular SGs with an oblate shape mainly extending in the xy-plane, ϕ_{SG} assuming a spherical shape may overestimate the actual volume. Such irregular shapes are more pronounced for larger SGs. Overall, we expect that our methods typically over- and underestimate ϕ_{SG}, respectively, and thus provide an estimate of the actual volume fraction.

Another source of error is the assignment of SGs to a given region of the cell based on the intensity of the respective reference cell at the centroid of the granule only and not assigning each voxel of a granule individually. In our case, regions of the cell with given $I/\langle I\rangle$ are multiple times larger than the average SG volume. Further, the distribution of intensities in the reference cells is smooth such that loss and gain of SG volume to adjacent regions is expected to be largely mitigated. In fact, yet half the width of intensity bins compared to those used in the calculation also yields consistent results; see Supplemental Fig. S15. We thus expect errors due to uncertainty in SG volume to be the dominant source of uncertainty in our calculation.

To calculate the average fraction of the total cytoplasm occupied by SGs, we consider the average total volume of SGs in live-cell experiments, see Fig. 2(f), and divide it by the average volume of the cell cytoplasm. We determine this volume using fixed cell data, taking advantage of the additional DAPI stain allowing to mask out the nucleus based on its 2D shape projected into 3D, and we find an average volume of the cell cytoplasm of 1380 $\mu\mathrm{m}^3$; see Fig. 3(d).

D. Live cell experiments

Live cell experiments were done using U2OS RDG3 cells. The protocols, however, are identical for either cell type.

Cells are plated on patterned coverslips as outlined above. Instead of a six-well plate, coverslips are mounted in a magnetic chamber that can be placed onto the microscope (Live Cell Instruments, Chamlide chambers CM-S22-4).

If live stains are used to stain the cytoskeleton, the cell media is switched to media containing the appropriate concentration of the stains at least 2 h before the start of experiments and about 1–2 h after plating the cells on the patterns. All live-cell experiments presented here were done using the recommended concentration for SPY-tubulin and SPY-FastAct cytoskeletal tags (Spirochrome). Note that SPY actin stains only f-actin. At the recommended concentration, Spirochrome claims no adverse effects in the cell.

1. Live cell imaging

Cells are imaged at 37 °C and 5% $\mathrm{CO_2}$ in normal cell media. Imaging is done on a Nikon Ti2 Eclipse microscope with a cage incubator and environmental chamber (both Okolabs), using a 100× oil objective with a numerical aperture of 1.49. Data are recorded using a Yokogawa CSU W1 spinning disk with a 50 μm pinhole size, together with a laser bench (Oxxius) including a 405 nm line at 180 mW, 488 nm and 561 nm at 200 mW, and a 640 nm line at 300 mW and a Photomerics Prime 95B camera. Together with the 100× objective, this gives a spatial resolution in the xy-plane of 0.11 μm per pixel. Note that the resolution limit is practically the same as on the setup used to image fixed cells. Due to the larger pixel size, however, we consider features with a size of two pixels (220 nm) optically resolved. Cells are imaged using Nikon's perfect focus system (PFS) to keep the cell in the focal plane.

The laser intensity is adjusted during trials to find a balance between induced phototoxicity and signal strength for each channel. Typically, six confocal stacks are recorded per cell at a spacing of 1 μm at 30 s intervals. Cells are treated with 150 μM arsenite to induce SGs. This is done by adding 3 μL of 50 mM arsenite to 1 mL of media in the chamlide chamber and subsequent careful stirring by pipetting several hundred μL of media up and down. A given experiment is started as soon as arsenite is added to the chamber. Note that this arsenite concentration is lower than the concentration used in fixed cell experiments (500 μM). This concentration has been determined throughout various trials to induce SGs in most cells while ensuring that cells withstand the stress and imaging for more than one hour. While the typical arsenite concentration in the literature is also 500 μM, it is not uncommon to use a lower concentration; see, e.g., Ref. [74]. The lower concentration suggests, however, that live-cell imaging, especially with a confocal microscope, is not free of artifacts and may induce further cell stress upon imaging.

Data from cells that exhibit odd behavior, including the presence of SGs in the absence of arsenite, abnormal changes in morphology, or detachment from the substrate, are discarded. In particular, temperatures in the incubation chamber on the microscope above 37 °C are observed to induce SGs. Such data are also discarded. When SGs exhibit unusual behavior, such as granulation or apparent hardening, at later times of arsenite treatment, the experimental data are cut multiple minutes before the onset of such changes in SG behavior to ensure consistency between experiments.

2. *Live cell data analysis*

Cells are analyzed using MATLAB code derived from the code used for fixed cells. The cell detection routine is modified such that the cell is tracked over time to account for drift in the xy-plane. We approximate the error of the drift correction over time to be ± one pixel. Cells are rotated such that the nucleus, or rather where we expect the nucleus to be based on the images of the actin and G3BP1 channel, falls onto the same side of the cell.

3. *Stress granule detection*

SGs are detected using the same routine as outlined above (Methods and Materials, Sec. IV C 5). We do not, however, perform the filtering step that discards SGs that are very close to each other in order to register SG coalescence and fusion. Also, the local contrast requirement is relaxed, considering granules where the surrounding is up to 70% as bright as the SG itself, to enhance detection of small and dim SGs, particularly at the onset of SG formation.

The calculation of SG volume is based on the SG detection by thresholding. The detected SG outline may deviate from the position of the maximum gradient in fluorescence intensity across the granule interface that is otherwise used to define the granule radius. The difference between the threshold-detected granule outline and the maximal gradient position is, however, small at -0.34 ± 0.69 pixel on average (see Methods and Materials, Sec. IV C 5). For the exemplary cell [Figs. 1(a)–1(c) and Figs. 2(a)–2(c)], we find a mean difference between the maximum of the intensity gradient and the threshold-detected interfaces of -0.27 pixel (0.018 μm), i.e., we overestimate slightly the SG volume.

4. *Reference construction*

Reference cells are constructed by local averaging. For live cell data, we do not have as rich information in the z-direction as in fixed cells as we only record data within the cell to minimize phototoxicity. Consequently, it is difficult to ensure good alignment in z and to accurately define the bottom of the cell. Reference cells for the live cell data are therefore not resolved in z but calculated by averaging of the maximum projections along z of the confocal stacks of a given cell at a given time. The time axis is aligned between cells such that $t_{\mathrm{SG}} = 0\,\mathrm{min}$ corresponds to the point in time when the first SGs are detected in a given cell. Pixels where more than half of the data from contributing cells have non-*NaN* entries are considered part of the reference cell, analogous to the construction of the reference cells for fixed cells. Note that the intensity normalization is not as precise as in fixed cells because the extent of the cell nucleus is not known, i.e., we cannot accurately define the cytoplasm, just the inside of the cell. The intensity of a given maximum projection of a given channel of a given cell at time t_{SG} is instead normalized by the average intensity across the maximum projection considering only the inside of the cell.

5. *Particle image velocimetry*

We performed particle image velocimetry (PIV) on the maximum projections of the actin and G3BP1 channel for each cell to extract the flow fields of actin and G3BP1 over time. PIV is done in MATLAB using code calling on functions from the MATLAB plug-in *PIVlab* [75]. The smallest interrogation window has a size of 8 by 8 pixels, i.e., 0.9 by 0.9 μm. To make use of the different cells we recorded, we average PIV results from individual cells, inspired by previous works [76]. For the averaging of the PIV results across different cells, each cell is masked by the respective cell outline, where pixels outside the cell are set to *NaN*. Further, we introduce a minimal contrast criterion to ensure reliability of the correlation analysis, which is the basis of PIV. For each interrogation window, we calculate the standard deviation of the local intensity. Only those windows are accepted that have a standard deviation 1.75 (4) times larger than the standard deviation in the background for the actin (G3BP1) channel. Windows that do not exceed this contrast measure are set to *NaN*. PIV results are further averaged by collecting data over time, binned in steps of 2.5 min. This method yields stacks of PIV results of up to 175 individual measurements. Finally, the PIV results are averaged across all measurements in a given window across cells and time to arrive at *PIV ensembles*. Windows in the PIV ensembles where less than 25% of the measurements contribute a non-*NaN* value are discarded. Note that the error in cell detection to correct for drift may cause errors in the PIV results. We estimate errors from the cell detection to be ±1 pixel. Assuming that the error is symmetric, however, we expect that averaging over many cells and time steps minimizes this error for the PIV analysis. We perform a similar analysis based on tracking of SGs, yielding consistent flow speeds; see Supplemental Fig. S11 [36].

Alignment between local actin and SG flow is calculated by projecting the local SG velocity vector ($\vec{SG}$) onto the actin velocity vector ($\vec{\text{actin}}$) using the dot product and normalizing by the magnitude of the actin velocity vector as in typical vector projection:

$$|\vec{SG}_{\parallel}| = \frac{\vec{SG}\cdot\vec{\text{actin}}}{|\vec{\text{actin}}|}.$$

This gives the amplitude of the local SG flow parallel to actin flow retaining the correct sign, i.e., flow in the opposite direction compared to actin flow is negative. The results are then spatially averaged over the entire cell. The magnitude of the orthogonal portion of $\vec{SG}$ is calculated analogously, only that the actin velocity is rotated by -90°.

6. Tracking of stress granules

Tracking of SGs is done using an established tracking function. The code considers the x-, y-, and z-coordinates, as well as R_{SG}, to identify the same SGs across frames. This code is based on the work of John C. Crocker from the University of Chicago, and it has been updated over time by Eric R. Dufresne and others (see online repositories in Ref. [77]).

E. Drug treatments

Cells are treated with nocodazole (Sigma-Aldrich, CAS 31430-18-9) at a concentration of 1.67 μM, jasplakinolide (Sigma-Aldrich, CAS 102396-24-7) at 50 nM, and blebbistatin (Sigma-Aldrich, CAS 856925-71-8) at 20 μM for 30 min before also adding arsenite to the media in order to ensure that the desired effect on the cytoskeleton is present in the cells at the onset of the stress response. The timing of 30 min was determined through live cell trials using SPY-FastAct and SPY-tubulin on drug-treated cells. Note that the time it takes for these drugs to take full effect on the cytoskeleton is comparable to the time it takes for stress granules to form and migrate towards the cell center. Separating drug treatment and arsenite treatment is therefore important in order to probe the effect of cytoskeletal perturbations on the entire process of SG formation and maturation.

ACKNOWLEDGMENTS

We thank Kathryn A. Rosowski for helpful discussions and assistance with cell culture, Nan Xue and Nicolas Bain for advice on using PIVlab, and all other laboratory members for fruitful discussions.

[1] S. F. Banani, H. O. Lee, A. A. Hyman, and M. K. Rosen, Biomolecular condensates: Organizers of cellular biochemistry, Nat. Rev. Mol. Cell Biol. **18**, 285 (2017).

[2] P. van Bergeijk, C. C. Hoogenraad, and L. C. Kapitein, Right time, right place: Probing the functions of organelle positioning, Trends Cell Biol. **26**, 121 (2016).

[3] S. Yadav and A. D. Linstedt, Golgi positioning, Cold Spring Harbor Perspect. Biol. **3**, a005322 (2011).

[4] M.-M. Fu and E. L. Holzbaur, Integrated regulation of motor-driven organelle transport by scaffolding proteins, Trends Cell Biol. **24**, 564 (2014).

[5] Z.-H. Sheng, Mitochondrial trafficking and anchoring in neurons: New insight and implications, J. Cell Biol. **204**, 1087 (2014).

[6] J. S. Bonifacino and J. Neefjes, Moving and positioning the endolysosomal system, Curr. Opin. Cell Biol. **47**, 1 (2017).

[7] A. A. Hyman, C. A. Weber, and F. Jülicher, Liquid-liquid phase separation in biology, Annu. Rev. Cell Dev. Biol. **30**, 39 (2014).

[8] N. L. Kedersha, M. Gupta, W. Li, I. Miller, and P. Anderson, RNA-binding proteins Tia-1 and Tiar link the phosphorylation of Eif-2α to the assembly of mammalian stress granules, J. Cell Biol. **147**, 1431 (1999).

[9] S. Jain, J. R. Wheeler, R. W. Walters, A. Agrawal, A. Barsic, and R. Parker, ATPase-modulated stress granules contain a diverse proteome and substructure, Cell **164**, 487 (2016).

[10] P. Anderson and N. Kedersha, Stress granules: The Tao of RNA triage, Trends Biochem. Sci. **33**, 141 (2008).

[11] D. W. Sanders, N. Kedersha, D. S. Lee, A. R. Strom, V. Drake, J. A. Riback, D. Bracha, J. M. Eeftens, A. Iwanicki, A. Wang, M.-T. Wei, G. Whitney, S. M. Lyons, P. Anderson, W. M. Jacobs, P. Ivanov, and C. P. Brangwynne, Competing protein-RNA interaction networks control multiphase intracellular organization, Cell **181**, 306 (2020).

[12] J. Guillén-Boixet, A. Kopach, A. S. Holehouse, S. Wittmann, M. Jahnel, R. Schlüßler, K. Kim, I. R. Trussina, J. Wang, D. Mateju, I. Poser, S. Maharana, M. Ruer-Gruß, D. Richter, X. Zhang, Y.-T. Chang, J. Guck, A. Honigmann, J. Mahamid, A. A. Hyman, R. V. Pappu, S. Alberti *et al.*, RNA-induced conformational switching and clustering of G3BP drive stress granule assembly by condensation, Cell **181**, 346 (2020).

[13] E. Kolobova, A. Efimov, I. Kaverina, A. K. Rishi, J. W. Schrader, A.-J. Ham, M. C. Larocca, and J. R. Goldenring, Microtubule-dependent association of AKAP350A and CCAR1 with RNA stress granules, Exp. Cell Res. **315**, 542 (2009).

[14] K. Fujimura, J. Katahira, F. Kano, Y. Yoneda, and M. Murata, Microscopic dissection of the process of stress granule assembly, Biochim. Biophys. Acta (BBA)–Mol. Cell Res. **1793**, 1728 (2009).

[15] N. C. Collier, J. Heuser, M. A. Levy, and M. J. Schlesinger, Ultrastructural and biochemical analysis of the stress granule in chicken embryo fibroblasts, J. Cell Biol. **106**, 1131 (1988).

[16] L. Nover, K. D. Scharf, and D. Neumann, Cytoplasmic heat shock granules are formed from precursor particles and are associated with a specific set of mRNAs, Mol. Cell. Biol. **9**, 1298 (1989).

[17] N. Kedersha, M. R. Cho, W. Li, P. W. Yacono, S. Chen, N. Gilks, D. E. Golan, and P. Anderson, Dynamic shuttling of Tia-1 accompanies the recruitment of mRNA to mammalian stress granules, J. Cell Biol. **151**, 1257 (2000).

[18] C. P. Brangwynne, C. R. Eckmann, D. S. Courson, A. Rybarska, C. Hoege, J. Gharakhani, F. Julicher, and A. A. Hyman,

Germline P granules are liquid droplets that localize by controlled dissolution/condensation, Science **324**, 1729 (2009).

[19] S. Saha, C. A. Weber, M. Nousch, O. Adame-Arana, C. Hoege, M. Y. Hein, E. Osborne-Nishimura, J. Mahamid, M. Jahnel, L. Jawerth, A. Pozniakovski, C. R. Eckmann, F. Jülicher, and A. A. Hyman, Polar positioning of phase-separated liquid compartments in cells regulated by an mRNA competition mechanism, Cell **166**, 1572 (2016).

[20] C. A. Weber, D. Zwicker, F. Jülicher, and C. F. Lee, Physics of active emulsions, Rep. Prog. Phys. **82**, 064601 (2019).

[21] A. W. Fritsch, A. F. Diaz-Delgadillo, O. Adame-Arana, C. Hoege, M. Mittasch, M. Kreysing, M. Leaver, A. A. Hyman, F. Jülicher, and C. A. Weber, Local thermodynamics govern formation and dissolution of *Caenorhabditis* elegans P granule condensates, Proc. Natl. Acad. Sci. USA **118**, e2102772118 (2021).

[22] Y. Shin, Y.-C. Chang, D. S. Lee, J. Berry, D. W. Sanders, P. Ronceray, N. S. Wingreen, M. Haataja, and C. P. Brangwynne, Liquid nuclear condensates mechanically sense and restructure the genome, Cell **175**, 1481 (2018).

[23] K. A. Rosowski, T. Sai, E. Vidal-Henriquez, D. Zwicker, R. W. Style, and E. R. Dufresne, Elastic ripening and inhibition of liquid–liquid phase separation, Nat. Phys. **16**, 422 (2020).

[24] K. E. Kasza, A. C. Rowat, J. Liu, T. E. Angelini, C. P. Brangwynne, G. H. Koenderink, and D. A. Weitz, The cell as a material, Curr. Opin. Cell Biol. **19**, 101 (2007).

[25] P. A. Ivanov, E. M. Chudinova, and E. S. Nadezhdina, Disruption of microtubules inhibits cytoplasmic ribonucleoprotein stress granule formation, Exp. Cell Res. **290**, 227 (2003).

[26] S. Kwon, Y. Zhang, and P. Matthias, The deacetylase HDAC6 is a novel critical component of stress granules involved in the stress response, Genes Develop. **21**, 3381 (2007).

[27] M. Loschi, C. C. Leishman, N. Berardone, and G. L. Boccaccio, Dynein and kinesin regulate stress-granule and P-body dynamics, J. Cell Sci. **122**, 3973 (2009).

[28] N.-P. Tsai, Y.-C. Tsui, and L.-N. Wei, Dynein motor contributes to stress granule dynamics in primary neurons, Neuroscience **159**, 647 (2009).

[29] E. S. Nadezhdina, A. J. Lomakin, A. A. Shpilman, E. M. Chudinova, and P. A. Ivanov, Microtubules govern stress granule mobility and dynamics, Biochim. Biophys. Acta (BBA)–Mol. Cell Res. **1803**, 361 (2010).

[30] K. G. Chernov, A. Barbet, L. Hamon, L. P. Ovchinnikov, P. A. Curmi, and D. Pastré, Role of microtubules in stress granule assembly: Microtubule dynamical instability favors the formation of micrometric stress granules in cells, J. Biol. Chem. **284**, 36569 (2009).

[31] T. J. Böddeker, K. A. Rosowski, D. Berchtold, L. Emmanouilidis, Y. Han, F. H. T. Allain, R. W. Style, L. Pelkmans, and E. R. Dufresne, Non-specific adhesive forces between filaments and membraneless organelles, Nat. Phys. **18**, 571 (2022).

[32] N. Kedersha, G. Stoecklin, M. Ayodele, P. Yacono, J. Lykke-Andersen, M. J. Fritzler, D. Scheuner, R. J. Kaufman, D. E. Golan, and P. Anderson, Stress granules and processing bodies are dynamically linked sites of mRNP remodeling, J. Cell Biol. **169**, 871 (2005).

[33] A. Aizer, Y. Brody, L. W. Ler, N. Sonenberg, R. H. Singer, and Y. Shav-Tal, The dynamics of mammalian P body transport, assembly, and disassembly in vivo, Mol. Biol. Cell **19**, 4154 (2008).

[34] Y.-C. Liao, M. S. Fernandopulle, G. Wang, H. Choi, L. Hao, C. M. Drerup, R. Patel, S. Qamar, J. Nixon-Abell, Y. Shen, W. Meadows, M. Vendruscolo, T. P. Knowles, M. Nelson, M. A. Czekalska, G. Musteikyte, M. A. Gachechiladze, C. A. Stephens, H. A. Pasolli, L. R. Forrest, P. St George-Hyslop, J. Lippincott-Schwartz, and M. E. Ward, RNA granules Hitchhike on lysosomes for long-distance transport, using Annexin a11 as a molecular tether, Cell **179**, 147 (2019).

[35] T. Ohn, N. Kedersha, T. Hickman, S. Tisdale, and P. Anderson, A functional RNAi screen links O-GlcNAc modification of ribosomal proteins to stress granule and processing body assembly, Nat. Cell Biol. **10**, 1224 (2008).

[36] See Supplemental Material at http://link.aps.org/supplemental/10.1103/PRXLife.1.023010 for additional results (e.g., side-views of reference cells or detailed results for all cytoskeletal perturbations), results from alternative methods (e.g., tracking of SGs), controls for all correlation analyses, as well as, Supplemental Movies.

[37] P. W. Oakes, S. Banerjee, M. C. Marchetti, and M. L. Gardel, Geometry regulates traction stresses in adherent cells, Biophys. J. **107**, 825 (2014).

[38] D. A. Weitz and M. Y. Lin, Dynamic scaling of cluster-mass distributions in kinetic colloid aggregation, Phys. Rev. Lett. **57**, 2037 (1986).

[39] C. P. Brangwynne, T. J. Mitchison, and A. A. Hyman, Active liquid-like behavior of nucleoli determines their size and shape in Xenopus laevis oocytes, Proc. Natl. Acad. Sci. USA **108**, 4334 (2011).

[40] J. R. Wheeler, T. Matheny, S. Jain, R. Abrisch, and R. Parker, Distinct stages in stress granule assembly and disassembly, eLife **5**, e18413 (2016).

[41] L. Jawerth, E. Fischer-Friedrich, S. Saha, J. Wang, T. Franzmann, X. Zhang, J. Sachweh, M. Ruer, M. Ijavi, S. Saha, J. Mahamid, A. A. Hyman, and F. Jülicher, Protein condensates as aging Maxwell fluids, Science **370**, 1317 (2020).

[42] F. Nédélec, T. Surrey, and E. Karsenti, Self-organisation and forces in the microtubule cytoskeleton, Curr. Opin. Cell Biol. **15**, 118 (2003).

[43] L. Blanchoin, R. Boujemaa-Paterski, C. Sykes, and J. Plastino, Actin dynamics, architecture, and mechanics in cell motility, Physiol. Rev. **94**, 235 (2014).

[44] A. Ponti, M. Machacek, S. L. Gupton, C. M. Waterman-Storer, and G. Danuser, Two distinct actin networks drive the protrusion of migrating cells, Science **305**, 1782 (2004).

[45] M. L. Gardel, B. Sabass, L. Ji, G. Danuser, U. S. Schwarz, and C. M. Waterman, Traction stress in focal adhesions correlates biphasically with actin retrograde flow speed, J. Cell Biol. **183**, 999 (2008).

[46] S. Fulda, A. M. Gorman, O. Hori, and A. Samali, Cellular stress responses: Cell survival and cell death, Int. J. Cell Biol. **2010**, 214074 (2010).

[47] T. P. Stossel, Contribution of actin to the structure of the cytoplasmic matrix, J. Cell Biol. **99**, 15s (1984).

[48] R. Niederman, P. C. Amrein, and J. Hartwig, Three-dimensional structure of actin filaments and of an actin gel made with actin-binding protein, J. Cell Biol. **96**, 1400 (1983).

[49] F. Fleischer, R. Ananthakrishnan, S. Eckel, H. Schmidt, J. Käs, T. Svitkina, V. Schmidt, and M. Beil, Actin network architecture

and elasticity in lamellipodia of melanoma cells, New J. Phys. **9**, 420 (2007).

[50] B. Gouveia, Y. Kim, J. W. Shaevitz, S. Petry, H. A. Stone, and C. P. Brangwynne, Capillary forces generated by biomolecular condensates, Nature (London) **609**, 255 (2022).

[51] M. J. De Brabander, R. M. Van de Veire, F. E. Aerts, M. Borgers, and P. A. Janssen, The effects of methyl (5-(2-thienylcarbonyl)-1H-benzimidazol-2-yl) carbamate, (R 17934; NSC 238159), a new synthetic antitumoral drug interfering with microtubules, on mammalian cells cultured in vitro, Cancer Res. **36**, 905 (1976).

[52] M. R. Bubb, I. Spector, B. B. Beyer, and K. M. Fosen, Effects of jasplakinolide on the kinetics of actin polymerization, J. Biol. Chem. **275**, 5163 (2000).

[53] G. S. Ou, Z. L. Chen, and M. Yuan, Jasplakinolide reversibly disrupts actin filaments in suspension-cultured tobacco BY-2 cells, Protoplasma **219**, 168 (2002).

[54] D. Van Goor, C. Hyland, A. W. Schaefer, and P. Forscher, The role of actin turnover in retrograde actin network flow in neuronal growth cones, PLoS ONE **7**, e30959 (2012).

[55] M. Feric and C. P. Brangwynne, A nuclear F-actin scaffold stabilizes ribonucleoprotein droplets against gravity in large cells, Nat. Cell Biol. **15**, 1253 (2013).

[56] M. Feric, C. P. Broedersz, and C. P. Brangwynne, Soft viscoelastic properties of nuclear actin age oocytes due to gravitational creep, Sci. Rep. **5**, 16607 (2015).

[57] J. Yi, X. S. Wu, T. Crites, and J. A. Hammer, Actin retrograde flow and actomyosin II arc contraction drive receptor cluster dynamics at the immunological synapse in Jurkat T cells, Mol. Biol. Cell **23**, 834 (2012).

[58] J. A. Ditlev, A. R. Vega, D. V. Köster, X. Su, T. Tani, A. M. Lakoduk, R. D. Vale, S. Mayor, K. Jaqaman, and M. K. Rosen, A composition-dependent molecular clutch between T cell signaling condensates and actin, eLife **8**, e42695 (2019).

[59] S. Murugesan, J. Hong, J. Yi, D. Li, J. R. Beach, L. Shao, J. Meinhardt, G. Madison, X. Wu, E. Betzig, and J. A. Hammer, Formin-generated actomyosin arcs propel T cell receptor microcluster movement at the immune synapse, J. Cell Biol. **215**, 383 (2016).

[60] R. Sakamoto, M. Tanabe, T. Hiraiwa, K. Suzuki, S. Ishiwata, Y. T. Maeda, and M. Miyazaki, Tug-of-war between actomyosin-driven antagonistic forces determines the positioning symmetry in cell-sized confinement, Nat. Commun. **11**, 3063 (2020).

[61] A. Hernández-Vega, M. Braun, L. Scharrel, M. Jahnel, S. Wegmann, B. T. Hyman, S. Alberti, S. Diez, and A. A. Hyman, Local nucleation of microtubule bundles through tubulin concentration into a condensed Tau phase, Cell Rep. **20**, 2304 (2017).

[62] S. U. Setru, B. Gouveia, R. Alfaro-Aco, J. W. Shaevitz, H. A. Stone, and S. Petry, A hydrodynamic instability drives protein droplet formation on microtubules to nucleate branches, Nat. Phys. **17**, 493 (2021).

[63] P. Anderson and N. Kedersha, RNA granules, J. Cell Biol. **172**, 803 (2006).

[64] F. De Leeuw, T. Zhang, C. Wauquier, G. Huez, V. Kruys, and C. Gueydan, The cold-inducible RNA-binding protein migrates from the nucleus to cytoplasmic stress granules by a methylation-dependent mechanism and acts as a translational repressor, Exp. Cell Res. **313**, 4130 (2007).

[65] M. Koguchi, K. Yamasaki, T. Hirano, and M. H. Sato, Vascular plant one-zinc-finger protein 2 is localized both to the nucleus and stress granules under heat stress in *Arabidopsis*, Plant Signal. Behav. **12**, e1295907 (2017).

[66] C. Guo, L. Chen, Y. Cui, M. Tang, Y. Guo, Y. Yi, Y. Li, L. Liu, and L. Chen, RNA binding protein OsTZF7 traffics between the nucleus and processing bodies/stress granules and positively regulates drought stress in rice, Front. Plant Sci. **13**, 802337 (2022).

[67] T. J. Böddeker, Physical Interactions of Membraneless Organelles with the Cytoskeleton, Ph.D. thesis, ETH Zurich, 2022.

[68] N. Kedersha and P. Anderson, Mammalian stress granules and processing bodies, Meth. Enzymol. **431**, 61 (2007).

[69] N. Kedersha, S. Tisdale, T. Hickman, and P. Anderson, Real-time and quantitative imaging of mammalian stress granules and processing bodies, Meth. Enzymol. **448**, 521 (2008).

[70] D. Berchtold, N. Battich, and L. Pelkmans, A systems-level study reveals regulators of membrane-less organelles in human cells, Mol. Cell **72**, 1035 (2018).

[71] G. Cox and C. J. Sheppard, Practical limits of resolution in confocal and non-linear microscopy, Microsc. Res. Tech. **63**, 18 (2004).

[72] P. Sengupta, T. Jovanovic-Talisman, D. Skoko, M. Renz, S. L. Veatch, and J. Lippincott-Schwartz, Probing protein heterogeneity in the plasma membrane using PALM and pair correlation analysis, Nat. Methods **8**, 969 (2011).

[73] S. L. Veatch, B. B. Machta, S. A. Shelby, E. N. Chiang, D. A. Holowka, and B. A. Baird, Correlation functions quantify super-resolution images and estimate apparent clustering due to over-counting, PLoS ONE **7**, e31457 (2012).

[74] A. Aulas, M. M. Fay, S. M. Lyons, C. A. Achorn, N. Kedersha, P. Anderson, and P. Ivanov, Stress-specific differences in assembly and composition of stress granules and related foci, J. Cell Sci. **130**, 927 (2017).

[75] W. Thielicke and R. Sonntag, Particle image velocimetry for MATLAB: Accuracy and enhanced algorithms in PIVlab, J. Open Res. Softw. **9**, 12 (2021).

[76] J. G. Santiago, S. T. Wereley, C. D. Meinhart, D. J. Beebe, and R. J. Adrian, A particle image velocimetry system for microfluidics, Exp. Fluids **25**, 316 (1998).

[77] https://site.physics.georgetown.edu/matlab/.